RESEARCH PAPER

Elastoplastic constitutive model for frozen sands based on framework of homogenization theory

De Zhang[1,2] · Enlong Liu[1,3] · Ji Huang[4]

Abstract

In this paper, the stress–strain responses of frozen sands and an elastoplastic constitutive model based on the homogenization theory of heterogeneous materials are presented. In the model, frozen soils are conceptualized as binary-medium materials consisting of bonded blocks and weak bands, and their mechanical behavior is described with elastic–brittle and elastoplastic constitutive models, respectively. By introducing two groups of parameters (i.e., the breakage ratio (λ_v and λ_s) and strain concentration coefficient (c_v and c_s) related to the spherical and deviatoric stress components), the proposed model incorporates the breakage process of ice crystals and nonuniform strain distributions between the matrix (bonded elements) and inclusions (frictional elements) of the heterogeneous frozen soil samples. Moreover, an elasticity-based model and a double hardening constitutive model are employed to simulate the mechanical properties of the bonded elements and the characteristics of the frictional elements, respectively. To provide appropriate and quantitative predictions with the binary-medium constitutive model proposed here, triaxial compression tests are performed on the frozen and unfrozen sands to determine the individual parameters at confining pressures of 300–1800 kPa. The model validations demonstrate that the predictions agree well with the available laboratory results.

Keywords Breakage ratio · Elastoplastic constitutive model · Frozen sands · Homogenization theory · Local strain concentration coefficient

1 Introduction

Frozen soils are special geological materials that are extensively distributed in cold regions; they are soils and rocks that contain some ice and have temperatures below 0 °C [1, 2]. Because these composite materials include solid mineral particulates, ice crystals, unfrozen water, and gaseous inclusions, the mechanical characteristics of frozen soils are clearly distinct from those of other geomaterials [3–7], such as rocks, concretes, shape memory alloys, and ceramics at room temperature. When the environmental temperature falls below the freezing point, the unfrozen water surrounding the soil particulates freezes gradually and transforms into ice crystals, thereby bonding the soil skeletons together and exhibiting a quasi-elastic–brittle behavior [8]. Constitutive models can be used to represent the macroscopic stress–strain responses; many existing constitutive models focus on the external factors such as the stress level, stress history, confining pressures, temperatures, loading rates, and soil types and place less emphasis on the changes in the internal configurations such as the interactions between the soil matrix and inclusions with different volume fractions, shapes, and orientations. However, regarding frozen soils, few research studies have considered the mesoscopic perspective, that is, they have not considered the micromechanisms between multiple ingredients of the compound soils. Therefore, establishing

✉ Enlong Liu
  liuenlong@lzb.ac.cn

1   State Key Laboratory of Frozen Soil Engineering, Northwest Institute of Eco-Environment and Resources, Chinese Academy of Sciences, Lanzhou 730000, China

2   University of Chinese Academy of Sciences, Beijing 100049, China

3   State Key Laboratory of Hydraulics and Mountain River Engineering, College of Water Resource and Hydropower, Sichuan University, Chengdu 610065, China

4   Institute of Disaster Management and Reconstruction, Sichuan University, Chengdu 610207, China

a micromechanics-based constitutive model for frozen soils is crucial.

Experimental and theoretical investigations of composite-reinforced soils are becoming increasingly prevalent in geotechnical engineering, and great progress has been made in predicting the effective mechanical behavior of such compound materials. In addition, the interactions between the soil matrix and inclusions with different volume fractions, shapes, and configurations have often been studied [9–11]. The existing models consider the constitutive relationships of each phase and combine them to predict the available laboratory results of the compound materials. For instance, Zhou et al. [12] formulated a strength upscaling model based on the yield design theory and linear comparison composite approach to estimate the macroscopic strength of nonlinear matrix–inclusion composites with different strength characteristics of the matrix and inclusions. Nguyen et al. [13] proposed a critical-state-based constitutive model for the behavior of clay treated with cement and fibers. This model simulates the behavior of these types of improved composite soils and the cementation degradation and fiber failure during the experiment advancement. Moreover, Dejaloud et al. [14] established a combined constitutive model for municipal solid wastes by considering an anisotropic critical-state-based constitutive model for matrix-phase-based materials and a von Mises-type model for fiber-phase-based materials based on the micromechanical theories of the volumetric homogenization procedure. Zhou et al. [15] proposed a multi-scale homogenization model for the strength prediction of fully and partially frozen soils by considering three material phases: the solid particle phase, crystal ice phase, and liquid water phase with their individual constitutive models. However, the previously mentioned models are unsuitable for frozen soils. The existing constitutive models cannot be applied to multi-phase materials and mainly focus on simulating the stress–strain responses from a phenomenological perspective based on the plasticity or thermodynamic theory. For instance, Lai et al. [16] proposed a yield surface by considering the strengthening and weakening effects of frozen sandy soils; they employed the experimental method to establish the elastoplastic model based on the plasticity theory. Furthermore, Lai et al. [17] proposed an elastoplastic constitutive model for frozen silty soils based on the generalized plastic theory by incorporating the plastic shear mechanism and volumetric compression mechanism; in addition, a dilatation yield surface was employed based on the experimental results. Lai et al. [18] presented a new systematical approach for deriving the yield criterion and flow rule of frozen soils based on the plasticity theory and dissipation function (homogenous function) to predict the pressure melting/crushing phenomenon of ice crystals.

Moreover, Ghoreishian et al. [19] established an elastoplastic constitutive model for describing the stress–strain features of saturated frozen soils and investigated the influence of the ice content and temperature; the predicted values confirmed the capability of the model. Lai et al. [20] formulated a double-yield surface model that considers the rotational hardening characteristics of frozen saline sandy soil and the initial and loaded anisotropies by employing the thermodynamic theories and non-associated flow rule. Xu et al. [21] presented a hypo-plasticity constitutive model for the viscous behavior of frozen soil, and Zhou et al. [22] applied the hyper-plasticity theory with multiple internal variables to establish a rate-dependent constitutive model based on the laboratory results of frozen loess. Furthermore, Loria et al. [23] proposed an elastoplastic constitutive model for capturing the nonlinear mechanical behavior of frozen silt based on the associated flow rules; they employed an elliptical and a parabolic yield surface to describe the volumetric mechanisms. However, few constitutive models incorporate the breakage and deformation mechanisms of multi-phase frozen soils based on the mesoscale level.

Research studies on constitutive models for reconstituted soils have led to satisfactory models, such as the Cam-Clay model [24–26], generalized plastic mechanics model [16, 27], unified hardening model [28–30], cemented Cam-Clay model [31], and other constitutive models [32–34, 56]. However, certain constitutive models have difficulties in modeling the strain softening and volumetric dilatation features. Therefore, some of them have been reformulated and improved by considering the influences of the soil structures (e.g., the revised structural Cam-Clay model [35], disturbed-state concept (DSC) model [36–38], thermo-poromechanics-based elastoplastic model [8], and some micromechanics-based models [39–41]). The structured soils usually possess different spatial arrangements and cementations, and their mechanical features differ much from those of remolded soils [42]. Because of the ice crystals, frozen soils possess stronger cementation bonds than general structured soils and exhibit strong structural performances and quasi-brittle characteristics. Therefore, they are classified as special "structured soils." Under an external load and based on the environmental circumstances, the cementations (ice crystals) between the soil particles break gradually and approach a completely deteriorated state, i.e., remolded soils without ice crystals are formed. In a model based on traditional meso-mechanics, the soil matrix, inclusions, and unfrozen water must be considered, which will enable the constitutive models more sophisticated, and thus, fewer researchers focus on the micromechanics-based constitutive model of frozen soils.

Ice crystals are special inclusions embedded in frozen soil samples; they exhibit a quasi-elastic behavior under

relatively weak deformations and break when the intergranular stress exceeds the failure stress of the ice crystals; this is accompanied by an elastoplastic behavior and strain softening phenomena. Under an external load, ice crystals break gradually and transform into unfrozen water (the pressure melting phenomenon) [16, 17, 43]. However, the existing constitutive models do not reflect the pressure melting phenomenon. To model the mechanical responses of frozen soils from a mesoscopic perspective, a new revised model for simulating the elastoplastic behavior is proposed based on the homogenization theory for heterogeneous materials [44–46]. The model conceptualizes geomaterials into binary media that consist of bonded blocks and weakened bands; the former are simplified as elastic–brittle elements (bonded elements), whereas the latter are regarded as elastoplastic elements (frictional elements). The bonded elements transform gradually into frictional elements owing to the structural breakage and cementation loss of the bonded blocks under external loading. More specifically, the bonded elements represent soil samples under infinitely low-stress conditions or in the undamaged state, whereas the frictional elements represent fully damaged frozen soil samples or remolded soils without ice crystals. Under intermediate stress conditions, the bonded and frictional elements combine their resistances to bear the external load [47]. The presented constitutive model is revised and reformulated based on the DSC model in the framework of the homogenization theory by incorporating the micromechanical characteristics and nonuniform strain between the bonded elements and representative volume element (RVE) [48–50]. Without considering the microstrain distributions and local breakage processes, some other constitutive models have also been investigated based on different theories [51–56]. The proposed model contributes its mutual influences on the independent binary media and considers the breakage process between the bonded and frictional elements. By decomposing the stress into hydrostatic and deviatoric components, the deformation mechanisms (compressive and shear mechanisms) can be easily determined. In addition, an elastic–brittle model is applied for the bonded elements, and a double hardening model is used for the frictional elements. The strain concentration coefficient represents the interior nonuniform strain distribution and the deformation relationship between the bonded and frictional elements.

2 Proposed constitutive model

2.1 Introduction to proposed model

The homogenization theory is applicable to compound soils and heterogeneous geomaterials [57]. In the RVE, the local stress is represented by Cartesian coordinates (x, y, z); it represents the overall characteristics of the composite soil, including the matrix and inclusions from a microscopic viewpoint. The stress and strain are considered homogeneous in the element volume fraction owing to the assumed micro-stress and strain. Therefore, the macroscopic average stress σ_{ij} and strain ε_{ij} in the total volume are expressed as follows:

$$\sigma_{ij} = \frac{1}{V} \int_V \sigma_{ij}^{\mathrm{loc}}(x, y, z) \mathrm{d}V, \tag{1}$$

$$\varepsilon_{ij} = \frac{1}{V} \int_V \varepsilon_{ij}^{\mathrm{loc}}(x, y, z) \mathrm{d}V, \tag{2}$$

where $\sigma_{ij}^{\mathrm{loc}}$ and $\varepsilon_{ij}^{\mathrm{loc}}$ are the local stress and strain, respectively.

The frozen soils (multi-phase geomaterials) are treated as porous media with three components: the soil skeleton, ice crystals, and unfrozen water, as illustrated in Fig. 1. The novelty of the proposed model is that, in the virgin stress state, frozen soils are considered fully intact without damage under saturated conditions; they only contain two components (soil particles and ice crystals; no unfrozen water). In the failure stress state, the ice crystals are assumed to have completely been melted into unfrozen water, which is the fully damaged state. The virgin stress state of the frozen soil specimen is conceptualized as bonded elements, and the fully damaged state including the soil skeleton and unfrozen water is idealized as frictional elements.

To illustrate the advantages of the proposed model, combined mechanical components are employed to account for the deformation mechanisms. The soil specimen is considered a hybrid of bonded blocks (bonded elements) and weak bands (frictional elements), which bear the external load collectively. As previously mentioned, the bonded elements consist of the ice crystals and soil skeleton with elastic–brittle mechanical properties; they are replaced by a spring E and brittle bond q in Fig. 2a. The brittle bond is completely rigid when the stress level is below the failure strength σ^b of the bonded elements and breaks/ruptures when the stress exceeds σ^b at an infinite strain. The frictional elements contain unfrozen water and the soil skeleton, in which the bond/cementation of the ice crystals is completely diminished and therefore negligible. The mechanical properties of the frictional elements are
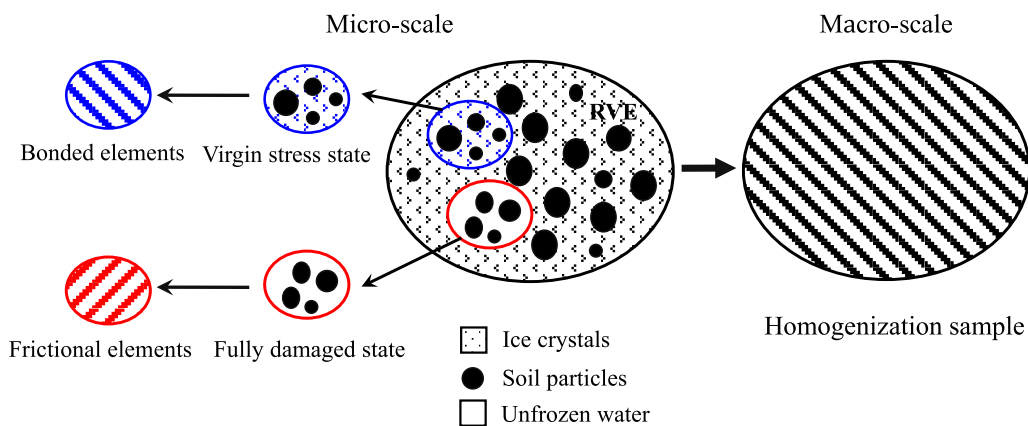
Fig. 1 Homogenization process of frozen soils in the framework of binary-medium model
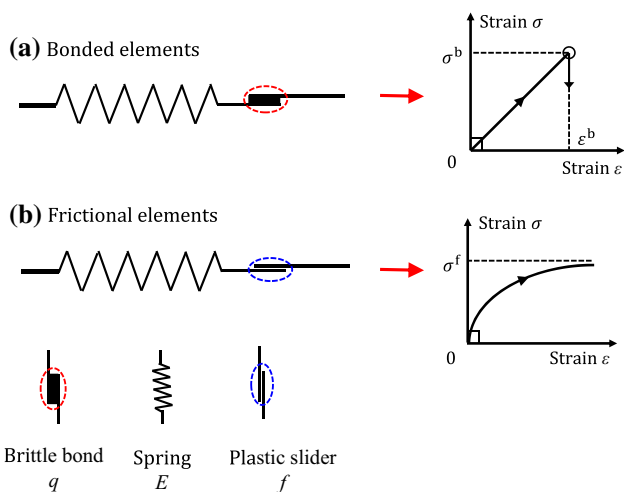

Fig. 2 Schematic description of the components of binary-medium model: **a** bonded elements, **b** frictional elements

similar to those of remolded soils and can be simulated with the spring E and plastic slider f in Fig. 2b.

2.2 Homogenization technique

Based on the homogenization theory [57], the bonded elements are used as the matrix and the frictional elements as the inclusions. The volumetric homogenization technique can relate the microscopic stress to the macroscopic stress; the specific procedure is presented in the following sections. On the microlevel, the stress and strain of the bonded elements are expressed as follows:

$$\sigma_{ij}^b = \frac{1}{V^b} \int_{V^b} \sigma_{ij}^{loc}(x,y,z)dV \text{ and } \varepsilon_{ij}^b = \frac{1}{V^b} \int_{V^b} \varepsilon_{ij}^{loc}(x,y,z)dV,$$

(3)

where V^b is the volume of the bonded elements for the RVE.

Likewise, the stress and strain of the frictional elements (from a microscopic viewpoint) are expressed as follows:

$$\sigma_{ij}^f = \frac{1}{V^f} \int_{V^f} \sigma_{ij}^{loc}(x,y,z)dV \text{ and } \varepsilon_{ij}^f = \frac{1}{V^f} \int_{V^f} \varepsilon_{ij}^{loc}(x,y,z)dV,$$

(4)

where V^f is the volume of the frictional elements for the RVE.

By substituting Eqs. (3) and (4) into Eqs. (1) and (2), the macroscopic average stress and strain can be reformulated as follows:

$$\sigma_{ij} = \frac{1}{V} \int_{V^b+V^f} \sigma_{ij}^{loc}(x,y,z)dV = \frac{V^b}{V}\frac{1}{V^b} \int_{V^b+V^f} \sigma_{ij}^{loc}(x,y,z)dV^b$$

$$+ \frac{V^f}{V}\frac{1}{V^f} \int_{V^b+V^f} \sigma_{ij}^{loc}(x,y,z)dV^b$$

$$+ \frac{V^f}{V}\frac{1}{V^f} \sigma_{ij}^{loc}(x,y,z)dV^f = \frac{V^b}{V}\sigma_{ij}^b + \frac{V^f}{V}\sigma_{ij}^f,$$

(5)

$$\varepsilon_{ij} = \frac{1}{V} \int_{V^b+V^f} \varepsilon_{ij}^{loc}(x,y,z)dV = \frac{V^b}{V}\frac{1}{V^b} \int_{V^b} \varepsilon_{ij}^{loc}(x,y,z)dV^b$$

$$+ \frac{V^f}{V}\frac{1}{V^f} \int_{V^f} \varepsilon_{ij}^{loc}(x,y,z)dV^f = \frac{V^b}{V}\varepsilon_{ij}^b + \frac{V^f}{V}\varepsilon_{ij}^f.$$

(6)

The volume fraction of the bonded elements and RVE is defined as $\lambda = \frac{V^f}{V}$, and the macroscopic average stress in Eq. (5) is rewritten as follows:

$$\sigma_{ij} = (1-\lambda)\sigma_{ij}^b + \lambda\sigma_{ij}^f.$$

(7)

Likewise, the macroscopic average strain becomes

$$\varepsilon_{ij} = (1-\lambda)\varepsilon_{ij}^b + \lambda\varepsilon_{ij}^f.$$

(8)

Owing to the failure patterns in the frozen soil elements, one is related to the volumetric compression due to the spherical stress, and the other is related to the shear yielding due to the deviatoric stress. To consider these two failure mechanisms accurately, the stress is decomposed into a hydrostatic/spherical pressure σ_m and deviatoric stress σ_s, and the corresponding strain is separated into a volumetric strain ε_v and generalized shear strain ε_s, as illustrated in Fig. 3.

Thus, the stress expression in Eq. (7) can be decomposed into hydrostatic and deviatoric components:

$$\sigma_m = (1 - \lambda_v)\sigma_m^b + \lambda_v \sigma_m^f, \tag{9}$$

$$\sigma_s = (1 - \lambda_v)\sigma_s^b + \lambda_v \sigma_s^f. \tag{10}$$

Similarly, the average strain in Eq. (8) is decomposed into

$$\varepsilon_v = (1 - \lambda_v)\varepsilon_v^b + \lambda_v \varepsilon_v^f, \tag{11-1}$$

$$\varepsilon_s = (1 - \lambda_s)\varepsilon_s^b + \lambda_s \varepsilon_s^f, \tag{11-2}$$

where λ_v and λ_s are the volume fraction related to the spherical components and the area fraction related to the deviatoric part, respectively.

The spherical and deviatoric components are defined as follows:

$$\sigma_m = \frac{1}{3}\sigma_{kk}, \tag{12-1}$$

$$\sigma_s = \sqrt{\frac{3}{2}\left(\sigma_{ij} - \frac{1}{3}\delta_{ij}\sigma_{kk}\right)\left(\sigma_{ij} - \frac{1}{3}\delta_{ij}\sigma_{kk}\right)}, \tag{12-2}$$

$$\varepsilon_v = \varepsilon_{kk}, \tag{12-3}$$

$$\varepsilon_s = \sqrt{\frac{2}{3}\left(\varepsilon_{ij} - \frac{1}{3}\delta_{ij}\varepsilon_{kk}\right)\left(\varepsilon_{ij} - \frac{1}{3}\delta_{ij}\varepsilon_{kk}\right)}, \tag{12-4}$$
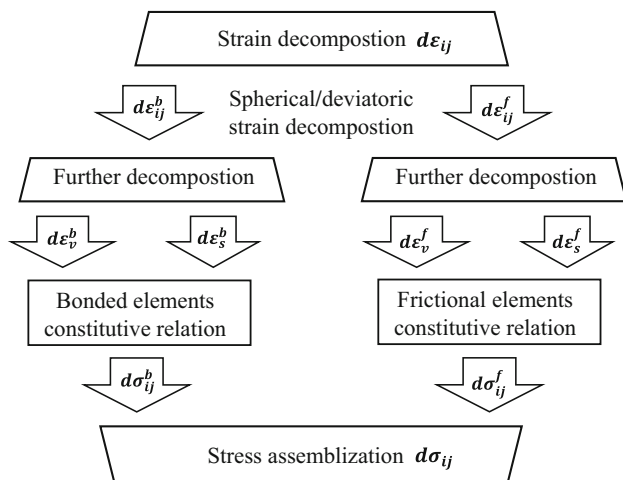
where δ_{ij} is the Kronecker function; $\sigma_{kk} = \sigma_1 + \sigma_2 + \sigma_3$; σ_1, σ_2, and σ_3 are the maximal principal stress, intermediate principal stress, and minimal principal stress, respectively; ε_1, ε_2, and ε_3 are the corresponding principal strains; and $\varepsilon_{kk} = \varepsilon_1 + \varepsilon_2 + \varepsilon_3$.

Based on Eqs. (9) and (11-1), the incremental expressions for the hydrostatic stress are rewritten as follows:

$$d\sigma_m = (1 - \lambda_v^0)d\sigma_m^b + \lambda_v^0 d\sigma_m^f + d\lambda_v(\sigma_m^{f0} - \sigma_m^{b0}), \tag{13}$$

$$d\varepsilon_v = (1 - \lambda_v^0)d\varepsilon_v^b + \lambda_v^0 d\varepsilon_v^f + d\lambda_v(\varepsilon_v^{f0} - \varepsilon_v^{b0}). \tag{14}$$

Based on Eqs. (10) and (11-2), the incremental expressions for the deviatoric stress are as follows:

$$d\sigma_s = (1 - \lambda_s^0)d\sigma_s^b + \lambda_s^0 d\sigma_s^f + d\lambda_s(\sigma_s^{f0} - \sigma_s^{b0}), \tag{15}$$

$$d\varepsilon_s = (1 - \lambda_s^0)d\varepsilon_s^b + \lambda_s^0 d\varepsilon_s^f + d\lambda_s(\varepsilon_s^{f0} - \varepsilon_s^{b0}), \tag{16}$$

where the superscript "0" represents the current stress/strain state. Figure 4 presents the incremental forms of the proposed model. In the incremental step from position A to B, the coordinate A is considered the current stress/strain state and B the stress/strain state after the incremental completion. In addition, the stress state B is completed by the current stress state A and infinitesimal stress increment $(d\sigma)$.

To construct a macroscopic constitutive model, the mechanical properties of the bonded and frictional elements should be considered (the individual relationship is linked with the strain concentration coefficient).

The bonded elements consist of soil particles and ice crystals, which are considered quasi-brittle materials owing to the cementation loss of the ice crystals. Therefore, an elastic-based constitutive model is used to predict the mechanical behavior of the bonded elements; the incremental equations are expressed as follows:

$$d\sigma_m^b = K^b d\varepsilon_v^b, \tag{17}$$

$$d\sigma_s^b = 3G^b d\varepsilon_s^b. \tag{18}$$

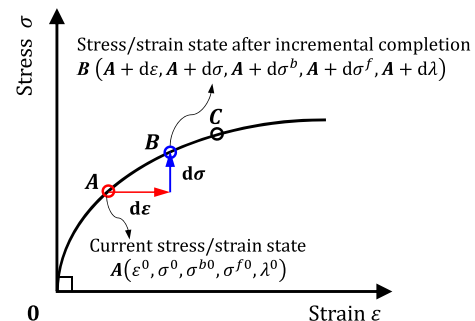Fig. 3 Strain decomposition of bonded elements and frictional elements

Fig. 4 Schematic description of incremental relationship in the binary-medium model

The frictional elements consist of soil particulates and unfrozen water, and their mechanical properties are seriously influenced by the sliding, rotation, and slippage of the soil particles. This can be described based on the plasticity theory and critical-state soil mechanics Roscoe et al. [24]. In this paper, a double hardening elastoplastic constitutive model [58, 59] was employed to simulate the deformation behavior of the frictional elements to model the strain softening and volumetric dilatancy. The respective incremental expressions are as follows:

$$d\sigma_m^f = L_{mm}^f d\varepsilon_v^f + L_{ms}^f d\varepsilon_s^f, \tag{19}$$

$$d\sigma_s^f = L_{sm}^f d\varepsilon_v^f + L_{ss}^f d\varepsilon_s^f, \tag{20}$$

where L_{mm}^f, L_{ms}^f, L_{sm}^f, and L_{ss}^f are the stiffness components of the frictional elements.

By substituting Eqs. (17)–(20) into Eqs. (13) and (15), the incremental expressions related to the spherical and deviatoric stresses can be rewritten as follows:

$$d\sigma_m = \left(1 - \lambda_v^0\right)K^b d\varepsilon_v^b + \lambda_v^0\left(L_{mm}^f d\varepsilon_v^f + L_{ms}^f d\varepsilon_s^f\right) + d\lambda_v\left(\sigma_m^{f0} - \sigma_m^{b0}\right), \tag{21}$$

$$d\sigma_s = \left(1 - \lambda_s^0\right)3G^b d\varepsilon_s^b + \lambda_s^0\left(L_{sm}^f d\varepsilon_v^f + L_{ss}^f d\varepsilon_s^f\right) + d\lambda_s\left(\sigma_s^{f0} - \sigma_s^{b0}\right). \tag{22}$$

In the homogenization theory, the deformations between bonded elements, frictional elements, and the RVE are not equivalent, i.e., $\varepsilon_v^b \neq \varepsilon_v^f \neq \varepsilon_v$ or $\varepsilon_s^b \neq \varepsilon_s^f \neq \varepsilon_s$. Fortunately, in continuum micromechanics, the strain concentration tensor relates the microstrain of the bonded elements to the RVE. Thus, in the paper, by considering the compressive and shear mechanisms, the strain concentration coefficient is classified into c_v (hydrostatic component) and c_s (deviatoric component). Consequently,

$$\varepsilon_v^b = c_v\varepsilon_v \text{ and } \varepsilon_s^b = c_s\varepsilon_s. \tag{23}$$

Based on Eq. (23), the following incremental formulations are obtained:

$$d\varepsilon_v^b = \varepsilon_v^0 dc_v + c_v^0 d\varepsilon_v = B_v d\varepsilon_v, \tag{24-1}$$

$$d\varepsilon_s^b = \varepsilon_s^0 dc_s + c_s^0 d\varepsilon_s = B_s d\varepsilon_s, \tag{24-2}$$

where

$$B_v = c_v^0 + \frac{\partial c_v}{\partial \varepsilon_v}\varepsilon_v^0, \tag{25-1}$$

$$B_s = c_s^0 + \frac{\partial c_s}{\partial \varepsilon_s}\varepsilon_s^0. \tag{25-2}$$

Moreover, the breakage ratio should be introduced to describe the cementation loss of the ice crystals, which is divided into the volume breakage ratio λ_v and area breakage ratio λ_s based on the compressive and shear mechanisms. In the paper, λ_v is related to the volumetric strain,

which is subjected to hydrostatic stress, and λ_s is related to the generalized shear strain, which is subjected to deviatoric stress. Thus, the two breakage ratios are expressed as follows:

$$\lambda_v = f_1(\varepsilon_v) \text{ and } \lambda_s = f_2(\varepsilon_s), \tag{26}$$

where the functions f_1 and f_2 are related to the volumetric and shear strains, respectively.

Based on Eq. (26), the incremental expressions can be written as follows:

$$d\lambda_v = \frac{\partial f_1}{\partial \varepsilon_v}d\varepsilon_v = \chi_v d\varepsilon_v, \tag{27}$$

$$d\lambda_s = \frac{\partial f_2}{\partial \varepsilon_s}d\varepsilon_s = \chi_s d\varepsilon_s. \tag{28}$$

Furthermore, based on Eqs. (11-1) and (11-2), the volumetric and deviatoric increments of the frictional elements can be derived as follows:

$$d\varepsilon_v^f = \frac{1}{\lambda_v^0}\left\{d\varepsilon_v - \left(1 - \lambda_v^0\right)d\varepsilon_v^b - d\lambda_v\left(\varepsilon_v^{f0} - \varepsilon_v^{b0}\right)\right\}, \tag{29}$$

$$d\varepsilon_s^f = \frac{1}{\lambda_s^0}\left\{d\varepsilon_s - \left(1 - \lambda_s^0\right)d\varepsilon_s^b - d\lambda_s\left(\varepsilon_s^{f0} - \varepsilon_s^{b0}\right)\right\}. \tag{30}$$

Rewriting Eqs. (9) and (11-1) leads to

$$\sigma_m^{f0} - \sigma_m^{b0} = \frac{1}{\lambda_v^0}\left(\sigma_m^0 - \sigma_m^{b0}\right), \tag{31}$$

$$\varepsilon_v^{f0} - \varepsilon_v^{b0} = \frac{1}{\lambda_v^0}\left(1 - c_v^0\right)\varepsilon_v^0. \tag{32}$$

Likewise, rewriting Eqs. (10) and (11-2) results in

$$\sigma_s^{f0} - \sigma_s^{b0} = \frac{1}{\lambda_s^0}\left(\sigma_s^0 - \sigma_s^{b0}\right), \tag{33}$$

$$\varepsilon_s^{f0} - \varepsilon_s^{b0} = \frac{1}{\lambda_s^0}\left(1 - c_s^0\right)\varepsilon_s^0. \tag{34}$$

Finally, the incremental constitutive relations of Eqs. (21) and (22) are obtained as follows:

$$d\sigma_m = A_1 d\varepsilon_v + B_1 d\varepsilon_s, \tag{35-1}$$

$$d\sigma_s = A_2 d\varepsilon_v + B_2 d\varepsilon_s, \tag{35-2}$$

where

$$A_1 = \left(1 - \lambda_v^0\right)K^b B_v + L_{mm}^f\left\{1 - \left(1 - \lambda_v^0\right)B_v - \frac{1 - c_v^0}{\lambda_v^0}\chi_v\varepsilon_v^0\right\}, \tag{36-1}$$

$$B_1 = \frac{\lambda_v^0}{\lambda_s^0}L_{ms}^f\left\{1 - \left(1 - \lambda_s^0\right)B_s - \frac{1 - c_s^0}{\lambda_s^0}\chi_s\varepsilon_s^0\right\}, \tag{36-2}$$

$$A_2 = \frac{\lambda_s^0}{\lambda_v^0} L_{sm}^f \left\{ 1 - \left(1 - \lambda_v^0\right) B_v - \frac{1 - c_v^0}{\lambda_v^0} \chi_v \varepsilon_v^0 \right\}, \quad (36-3)$$

$$B_2 = \left(1 - \lambda_s^0\right) 3 G^b B_s$$
$$+ L_{ss}^f \left\{ 1 - \left(1 - \lambda_s^0\right) B_s - \frac{1 - c_s^0}{\lambda_s^0} \chi_s \varepsilon_s^0 \right\}$$
$$+ \left(\sigma_s^{f0} - \sigma_s^{b0}\right) \frac{\chi_s}{\lambda_s^0}. \quad (36-4)$$

In (35-1), (35-2), (36-1), (36-2), (36-3), and (36-4), there are four groups of parameters that must be set; the parameters of the bonded and frictional elements can be determined based on the experimental results of the frozen and unfrozen sands, breakage ratio, and local strain concentration coefficient, which are determined by the trial-and-error method based on the test data. The determination procedures of the parameters are described in the following sections.

3 Constitutive relations of bonded and frictional elements

According to Fig. 5, in the intact/virgin stress state, the samples contain undamaged soil particles and ice crystals, which are considered bonded elements with elastic–brittle characteristics. In the fully damaged stress state, the ice crystals in the soil samples are considered completely transformed into unfrozen water; the specimens contain only soil particulates and unfrozen water, which is

conceptualized as frictional elements with an elastoplastic behavior. The practical stress–strain curve for the stress state with partial damage conditions is marked in red in Fig. 6; evidently, both elements bear the external load.

3.1 Constitutive relations of bonded elements

On the meso-level, the bonded elements in the frozen soil samples have the following characteristics: (1) the cementation (ice crystals) between the soil skeleton bonds the soil particulates. Once the intergranular stress exceeds the failure strength of the bonded elements, the bond is rapidly broken, and the mechanical behavior of the bonded elements can be considered elastic–brittle; (2) after the bonded elements are destroyed, they are completely transformed into frictional elements. To model the mechanical properties of the bonded elements, an elastic and perfectly brittle constitutive model is adopted; the stiffness tensor L_{ijkl}^b is expressed as follows:

$$L_{ijkl}^b = \frac{1}{3} \left(3K^b - 2G^b\right) \delta_{ij}\delta_{kl} + G^b \left(\delta_{il}\delta_{jk} + \delta_{ik}\delta_{jl}\right), \quad (37)$$

where K^b is the bulk modulus and G^b the shear modulus of the bonded elements.

3.2 Constitutive relations of frictional elements

As mentioned in Sect. 2.1, the mechanical properties of the frictional elements are similar to those of the remolded soils; thus, an appropriate elastoplastic model is required. To describe the strain softening and volumetric dilatation
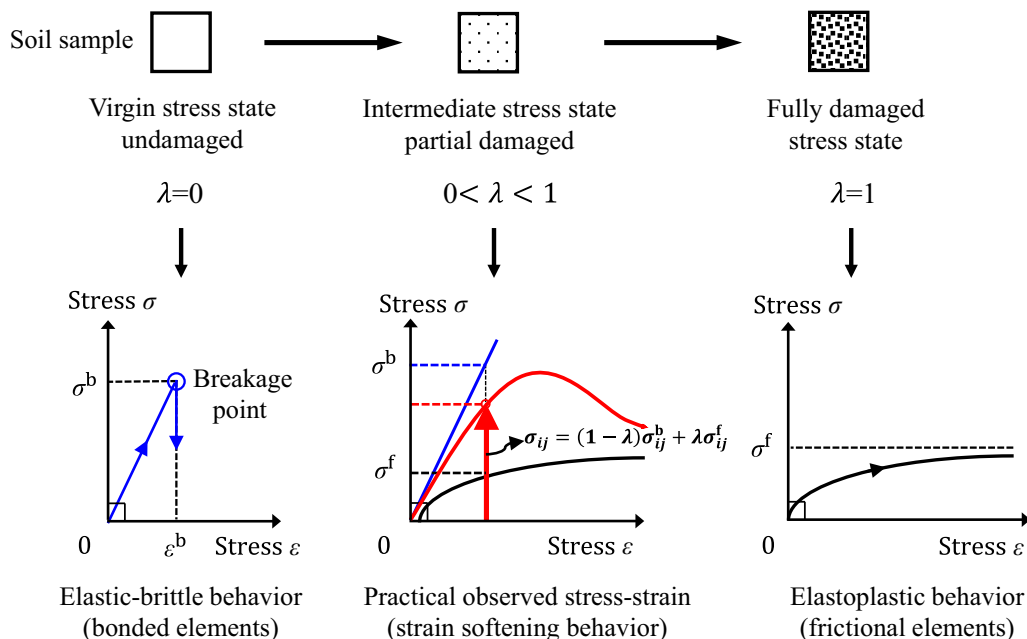

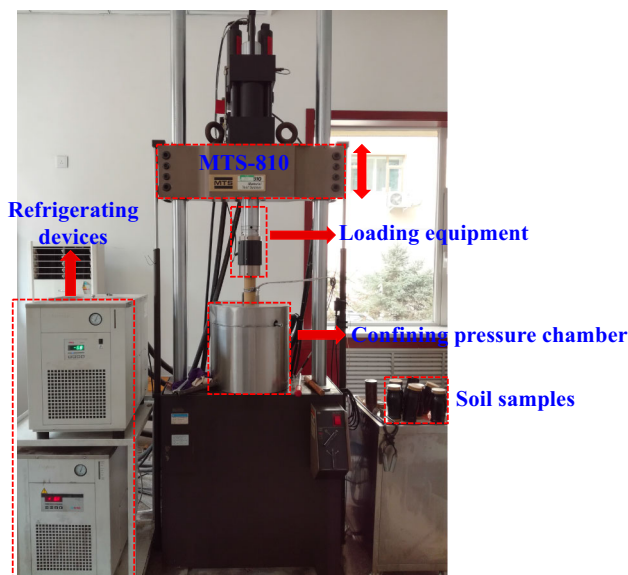**Fig. 5** Deformational process of frozen soils under external loads

Fig. 6 Modified material test system (MTS-810)

behavior of the unfrozen sands, a single yield surface with two hardening parameters is used to simulate the mechanical characteristics of the frictional elements [58, 59]. The mathematical expression is as follows:

$$f^f = \frac{\sigma_m^f}{1 - (\eta^f / \alpha)^n} - H, \tag{38}$$

where

$$\eta^f = \frac{\sigma_m^f}{\sigma_s^f}, \tag{39-1}$$

$$\sigma_m^f = \frac{1}{3}\left(\sigma_1^f + \sigma_2^f + \sigma_3^f\right), \tag{39-2}$$

$$\sigma_s^f = \sqrt{0.5\left[\left(\sigma_1^f - \sigma_2^f\right)^2 + \left(\sigma_1^f - \sigma_3^f\right)^2 + \left(\sigma_2^f - \sigma_3^f\right)^2\right]}, \tag{39-3}$$

$$\alpha = \alpha_0\left[1.0 - c_1 \exp\left(-\frac{\varepsilon_s^{pf}}{c_2}\right)\right], \tag{39-4}$$

$$H = H_0 \exp\left(\beta\varepsilon_v^{pf}\right), \tag{39-5}$$

where the superscript f represents the frictional elements and ε_v^{pf} and ε_s^{pf} denote the volumetric plastic strain and generalized shear plastic strain of the frictional elements, respectively; H is the hardening function; α_0, c_1, c_2, H_0, and β are the model parameters, which can be determined with the tested data of the unfrozen sands.

Moreover, a non-associated flow rule is employed, and the potential surface is presented as follows:

$$g^f = \frac{\sigma_m^f}{1 - (\eta^f / \alpha)^{n_1}} - H. \tag{40}$$

The incremental plastic volumetric strain and generalized shear strain are obtained based on the orthogonal flow rule:

$$d\varepsilon_v^{pf} = d\Lambda \frac{\partial g^f}{\partial \sigma_m^f} \text{ and } d\varepsilon_s^{pf} = d\Lambda \frac{\partial g^f}{\partial \sigma_s^f}, \tag{41}$$

where $d\Lambda$ is the plastic multiplier ($d\Lambda > 0$).

Based on the consistency condition, Eq. (38) can be rewritten as follows:

$$\frac{\partial f^f}{\partial \sigma_m^f}d\sigma_m^f + \frac{\partial f^f}{\partial \sigma_s^f}d\sigma_s^f + \frac{\partial f^f}{\partial \alpha}\frac{\partial \alpha}{\partial \varepsilon_s^{pf}}d\varepsilon_s^{pf} + \frac{\partial f^f}{\partial H}\frac{\partial H}{\partial \varepsilon_v^{pf}}d\varepsilon_v^{pf} = 0. \tag{42}$$

By rewriting Eqs. (41) and (42), the plastic multiplier is obtained:

$$d\Lambda = \frac{1}{h}\left(\frac{\partial f^f}{\partial \sigma_m^f}d\sigma_m^f + \frac{\partial f^f}{\partial \sigma_s^f}d\sigma_s^f\right) \tag{43-1}$$

and

$$\begin{aligned} h &= -\frac{\partial f^f}{\partial \alpha}\frac{\partial \alpha}{\partial \varepsilon_s^{pf}}\frac{\partial g}{\partial \sigma_s^f} - \frac{\partial f^f}{\partial H}\frac{\partial H}{\partial \varepsilon_v^{pf}}\frac{\partial g^f}{\partial \sigma_m^f} \\ &= \frac{n\sigma_m^f(\eta^f / \alpha)^n}{\alpha[1 - (\eta^f / \alpha)^n]^2}\frac{c_1}{c_2}\alpha_0 \exp\left(-\frac{\varepsilon_s^{pf}}{c_2}\right)\frac{\partial g^f}{\partial \sigma_s^f} \\ &\quad + H_0\beta \exp\left(\beta\varepsilon_v^{pf}\right)\frac{\partial g^f}{\partial \sigma_m^f}. \end{aligned} \tag{43-2}$$

Hence, the incremental constitutive model for the frictional elements is expressed as follows:

$$d\sigma_m^f = L_{mm}^f d\varepsilon_v^f + L_{ms}^f d\varepsilon_s^f, \tag{44-1}$$

$$d\sigma_s^f = L_{sm}^f d\varepsilon_v^f + L_{ss}^f d\varepsilon_s^f, \tag{44-2}$$

where

$$L_{mm}^f = \frac{1}{M}\left(\frac{1}{3G^f} + \frac{1}{h}\frac{\partial f^f}{\partial \sigma_s^f}\frac{\partial g^f}{\partial \sigma_s^f}\right); \quad L_{ms}^f = -\frac{1}{Mh}\frac{\partial f^f}{\partial \sigma_s^f}\frac{\partial g^f}{\partial \sigma_m^f}, \tag{45-1}$$

$$L_{sm}^f = -\frac{1}{Mh}\frac{\partial f^f}{\partial \sigma_m^f}\frac{\partial g^f}{\partial \sigma_s^f}; \quad L_{ss}^f = \frac{1}{M}\left(\frac{1}{K^f} + \frac{1}{h}\frac{\partial f^f}{\partial \sigma_m^f}\frac{\partial g^f}{\partial \sigma_m^f}\right), \tag{45-2}$$

$$M = \frac{1}{3G^f K^f} + \frac{1}{K^f h}\frac{\partial f^f}{\partial \sigma_s^f}\frac{\partial g^f}{\partial \sigma_s^f} + \frac{1}{3G^f h}\frac{\partial f^f}{\partial \sigma_m^f}\frac{\partial g^f}{\partial \sigma_m^f}, \tag{45-3}$$

$$\frac{\partial f^f}{\partial \sigma_m^f} = \frac{1 + (n-1)(\eta^f / \alpha)^n}{[1 - (\eta^f / \alpha)^n]^2}, \tag{45-4}$$

$$\frac{\partial f^f}{\partial \sigma_s^f} = \frac{n\eta^f(\eta^f / \alpha)^n}{[1 - (\eta^f / \alpha)^n]^2}, \tag{45-5}$$

$$\frac{\partial g^f}{\partial \sigma_m^f} = \frac{1 + (n_1 - 1)(\eta^f / \alpha)^{n_1}}{[1 - (\eta^f / \alpha)^{n_1}]^2}, \tag{45-6}$$

$$\frac{\partial g^f}{\partial \sigma_s^f} = \frac{n_1 \eta^f \left(\eta^f / \alpha\right)^{n_1}}{\left[1 - \left(\eta^f / \alpha\right)^{n_1}\right]^2} \cdots \qquad (45-7)$$

3.3 Breakage ratio

The occurrences of shear bands (micro-cracks, voids, and fracture) may cause the degradation of the geomaterial [60]. To capture the deterioration process accurately, the breakage ratio λ is used to describe the transition from bonded to frictional elements; their evolutionary regularity is similar to those of the hardening parameters of plasticity [27] and damage factors in continuum damage mechanics [61, 62]. Moreover, the breakage ratio is an internal variable on the mesoscale level and cannot be directly measured by laboratory tests, and the breakage ratio λ approaches zero when the soil sample is subjected to virgin loading. The reason for this is that the bonded elements do not break (no frictional elements) and bear the external load alone. With increasing stress amplitude, the bonded elements break gradually and transform into frictional elements. Hence, both elements bear the external intermediate load, and the breakage ratio λ increases and approaches 1. The following relations are proposed for the evolution of the volumetric breakage ratio λ_v and corresponding area breakage ratio λ_s:

$$\lambda_v = 1 - \rho_v \exp\left\{-k_v (\varepsilon_v)^{\theta_v}\right\}, \qquad (46-1)$$

$$\lambda_s = 1 - \rho_s \exp\left\{-\zeta_s (\varepsilon_s)^{r_s}\right\}. \qquad (46-2)$$

Combining Eqs. (27) and (28) leads to

$$\chi_v = \rho_v k_v \theta_v (\varepsilon_v)^{\theta_v - 1} \exp\left\{-k_v (\varepsilon_v)^{\theta_v}\right\}, \qquad (47-1)$$

$$\chi_s = \rho_s \zeta_s r_s (\varepsilon_s)^{r_s - 1} \exp\left\{-\zeta_s (\varepsilon_s)^{r_s}\right\}. \qquad (47-2)$$

3.4 Local strain concentration coefficient

The following relations are proposed based on the changes in the microscopic strain concentration coefficient:

$$c_v = \exp\left\{-\alpha_v (\varepsilon_v)^{m_v}\right\}, \qquad (48-1)$$

$$c_s = \exp\left\{-\beta_s (\varepsilon_s)^{n_s}\right\}. \qquad (48-2)$$

Combining Eqs. (24-1), (24-2), (25-1), and (25-2) results in

$$B_v = c_v^0 - \varepsilon_v^0 \alpha_v m_v (\varepsilon_v)^{m_v - 1} \exp\left\{-\alpha_v (\varepsilon_v)^{m_v}\right\}, \qquad (49-1)$$

$$B_s = c_s^0 - \varepsilon_s^0 \beta_s n_s (\varepsilon_s)^{n_s - 1} \exp\left\{-\beta_s (\varepsilon_s)^{n_s}\right\}. \qquad (49-2)$$

4 Determination of model parameters and validations

To validate the applicability of the proposed model, two triaxial laboratory test groups are performed. The first test group is conducted to investigate the mechanical behavior of the frozen sands at − 6 °C to determine the real stress–strain behavior of the frozen sands. The parameters of the bonded elements (e.g., the bulk and shear moduli) are identified based on the isotropic loading–unloading–reloading compression and loading–unloading–reloading compression tests at a very low axial strain. The second test group comprises conventional triaxial compression tests conducted on the unfrozen sand without ice crystals to determine the parameters of the frictional elements.

4.1 Test procedure of frozen sands

The tested materials are standard sands; the physical parameters are listed in Table 1. The specimens are prepared according to the GB/T50123-1999 Standard for Soil Test Method of the Ministry of Water Resources, China. The sands are added layer by layer into a copper mold (three components of equal volumes) to create cylindrical samples with inner diameters of 61.8 mm, heights of 125 mm, and a dry density of 1.78 g/cm³. Subsequently, porous stones are mounted on both ends of each specimen, which is then placed into a sealed vacuum barrel for 3 h. Furthermore, the sample is saturated for more than 12 h to ensure a saturation degree of more than 95%. Subsequently, the porous stones are substituted by epoxy resin platens. In the next step, the soil samples are quickly frozen in a refrigerator for more than 48 h at − 30 °C to prevent the formation of ice lenses. Then, the soil samples are covered with rubber membranes and placed into an incubator until their temperature reaches − 6 °C. Afterward, the triaxial compression tests are conducted in the modified MTS-810 configuration: The frozen samples are embedded in the pressure chamber (Fig. 6). In addition, the prepared specimens are isotropically loaded 5 min prior to the axial loading at confining pressures ranging from 300 to 1800 kPa. Two stress–strain conditions describe the failure of the soil specimens; regarding the strain hardening and strain softening curves, the peak stresses correspond to an

Table 1 Physical parameters of sands (unit %)

Composition of particulate diameter				
> 2.0 mm	1.0–2.0 mm	0.75–1.0 mm	0.5–0.75 mm	0.25–0.75 mm
5.32	11.63	19.52	25.17	38.36

axial strain of 15% and the maximal stress value, respectively. The loading rate is 1.25 mm/min, and the stress path and loading pattern are illustrated in Fig. 7. Figure 8 presents the samples after the tests. For convenience, a positive stress and strain are assumed under compression conditions.

The experimental results of the deviatoric stress–axial strain and volumetric strain–axial strain curves of the frozen sands are illustrated in Fig. 9a, b. All stress–strain curves exhibit strain softening, which becomes less evident with increasing confining pressure of 300–1800 kPa. This is because the bonds (ice crystals) between the soil particulates become gradually damaged at low confining pressures, and shear bands occur, as shown in Fig. 8a–c. However, the lateral deformation is severely restricted at a high confining pressure. Hence, the stress–strain curves exhibit a slight softening phenomenon accompanied by a failure pattern (bulging) in the center of the soil samples (Fig. 8d, e). The volumetric strain is first continuously compacted, and dilatancy occurs. According to the results, the lower the confining pressure, the more the specimen dilates.

4.2 Test procedure of unfrozen sands

The triaxial compression tests of the unfrozen sands under drained conditions are conducted by employing the triaxial system in Fig. 10. The tested materials and soil preparation method are similar to those of the frozen sands in Sect. 3.1. The dry densities of the unfrozen and frozen sand samples are equal; the diameter is 61.8 mm, and the height is 120 mm. After the sand sample is fully saturated, it is not frozen in the refrigerator; instead, it is covered with rubber membranes and inserted into the triaxial system to perform the triaxial compression tests.

The deviatoric stress–axial strain and volumetric strain curves of the unfrozen sands are presented in Fig. 11a, b. Because the soil samples do not contain ice crystals, their mechanical behavior is distinct from that of the frozen
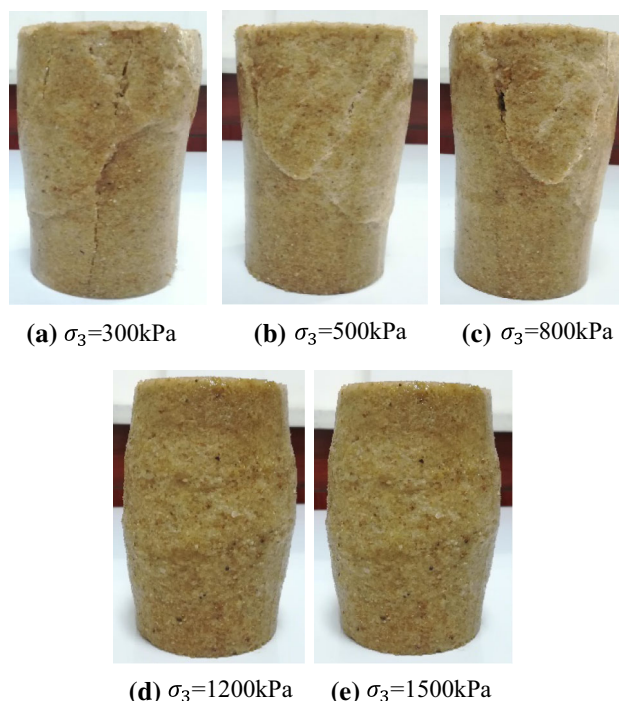

(a) σ_3=300kPa   **(b)** σ_3=500kPa   **(c)** σ_3=800kPa

(d) σ_3=1200kPa   **(e)** σ_3=1500kPa

Fig. 8 Failure patterns of frozen sands: **a** σ_3 = 300 kPa, **b** σ_3 = 500 kPa, **c** σ_3 = 800 kPa, **d** σ_3 = 1200 kPa, and **e** σ_3 = 1500 kPa

sands. In addition, the experimental results demonstrate that (1) the stress–strain curves exhibit a slight softening tendency at a confining pressure of 300 kPa, followed by a strain hardening phenomenon with increasing confining pressure; (2) at confining pressures of 300–800 kPa, the volumetric strain–axial strain curves meet under virgin load conditions and become separated until the soil samples fail. However, at confining pressures of 1200–1800 kPa, the volumetric curves are compacted until the volume of the soil sample remains constant in the critical stress state. The failure patterns are always bulged in the centers of the soil samples, as presented in Fig. 12a, b for all tested unfrozen sands.
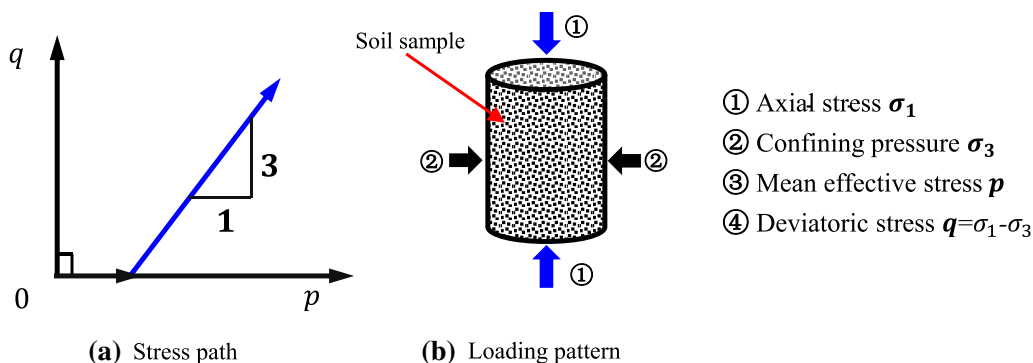

(a) Stress path   **(b)** Loading pattern

① Axial stress σ_1
② Confining pressure σ_3
③ Mean effective stress p
④ Deviatoric stress q=σ_1-σ_3

Fig. 7 Test procedures of frozen sands: **a** stress path, **b** loading pattern
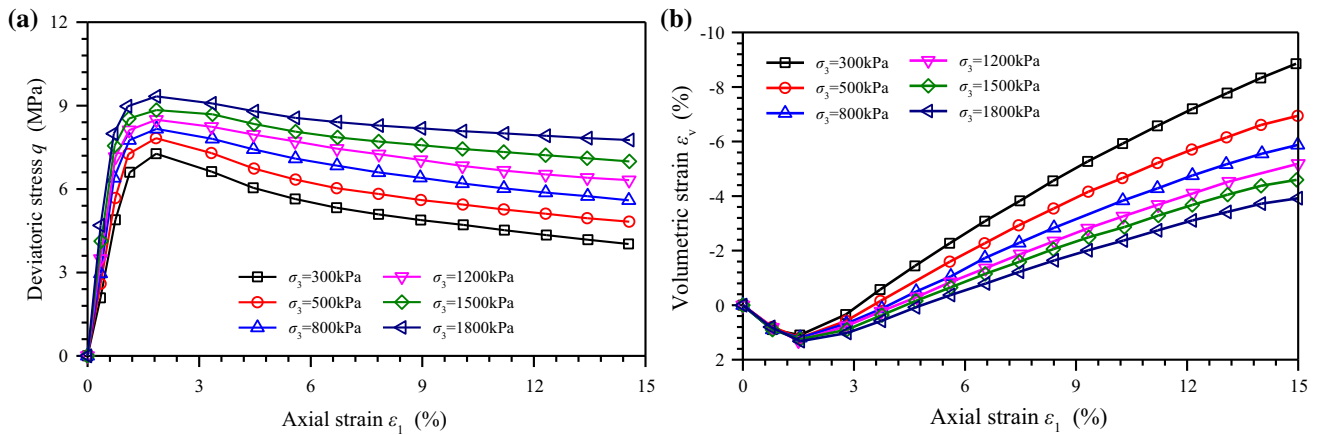
(a)

(b)

Fig. 9 Stress–strain curves of frozen sands: **a** deviatoric stress–axial strain curves, **b** volumetric strain–axial strain curves

Fig. 10 Triaxial test apparatus

4.3 Determination of model parameters

To determine the shear modulus G, loading–unloading–reloading triaxial shear tests are conducted at different confining pressures. The experimental results are shown in Fig. 13a, b, and the shear modulus is defined by $G = \frac{\mathrm{d}q}{3\mathrm{d}\varepsilon_s^e}$ owing to the

elastic behavior in the unloading process. It should be noted that the shear moduli of the bonded elements are determined when the generalized shear strain is below 1% (Fig. 13a); in this strain range, the bonded elements can be considered intact and without damage. In the nonlinear elastic model, the bulk modulus can be obtained by isotropic compression tests ($q = 0$) with loading–unloading–reloading cycles (defined by $K = \frac{\mathrm{d}p}{\mathrm{d}\varepsilon_v^e}$). As shown in Fig. 14a, b, different stress levels are applied to the frozen and unfrozen sands.

There are four groups of parameters: the material parameters related to the bonded elements and frictional elements (determined by experimental results) and the internal state variables of the breakage ratio and local strain concentration coefficient (determined by trial-and-error tests with laboratory data).

The parameters of the bonded elements are determined at an axial strain of 0.5% and based on the test results of the frozen sands: $K^b = 6531 P_a \left(\frac{\sigma_3}{P_a}\right)^{0.542}$, $G^b = 13280 P_a \left(\frac{\sigma_3}{P_a}\right)^{0.2213}$, P_a is 101.33 kPa.
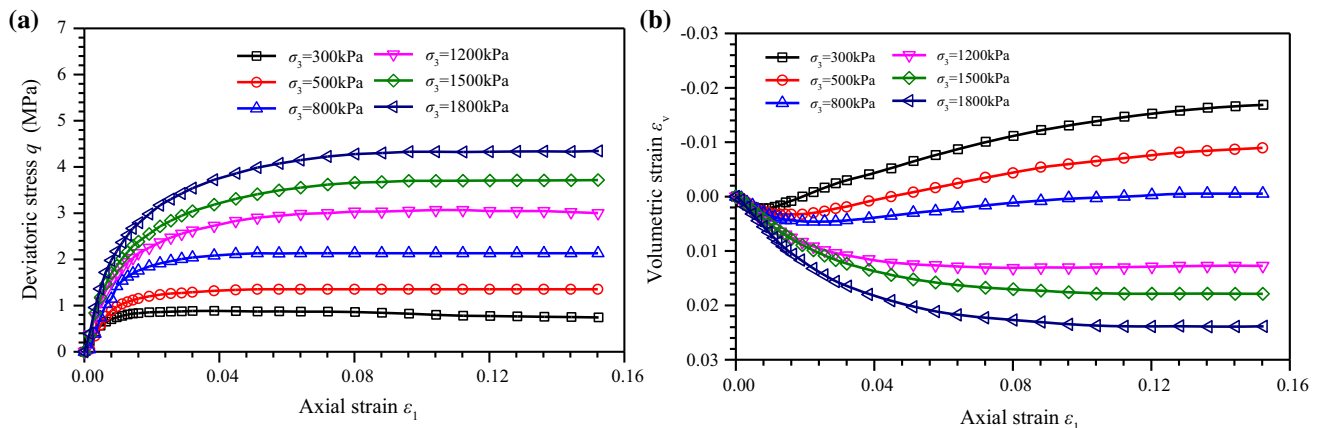
(a)

(b)

Fig. 11 Stress–strain curves of unfrozen sands: **a** deviatoric stress–axial strain curves, **b** volumetric strain–axial strain curves

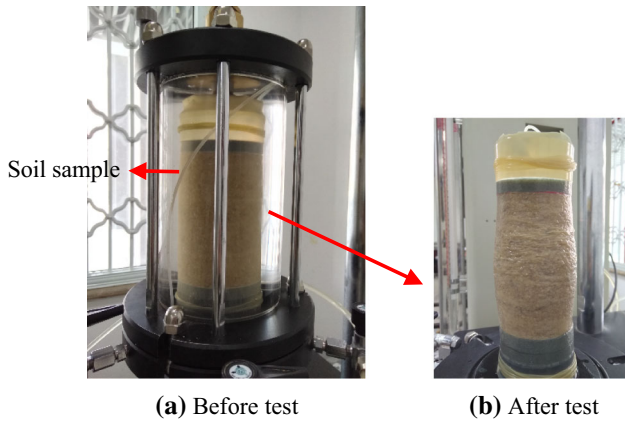**(a)** Before test   **(b)** After test

Fig. 12 Soil sample of unfrozen sands before and after tests

The parameters of the frictional elements are determined based on the laboratory results of the unfrozen sands in Sect. 4.2: $K^f = 950.2 P_a \left(\frac{\sigma_3}{P_a}\right)^{0.231}$, $G^f = 666 P_a \left(\frac{\sigma_3}{P_a}\right)^{0.2446}$, $n = 0.1$, $n_1 = 0.2$, $c_1 = 0.6$, $c_2 = 10$, $\beta = 40$, $H_0 = 350$, $\alpha_0 = 1.837 \left(\frac{\sigma_3}{P_a}\right)^{0.544}$.

The breakage ratio and local strain concentration coefficient are internal state variables and can be obtained by the trial-and-error method; thus, based on the test results: $k_v = 1 \, \text{at} \, \sigma_3 \leq 0.8 \, \text{MPa}$ and $k_v = 2 \, \text{at} \, \sigma_3 > 0.8 \, \text{MPa}$, $\theta_v = 2$, $\zeta_s = 120$, $r_s = 1.2$, $a_v = 1.0$, $m_v = 2.0$, $\beta_s = 1.0$, $n_s = 2.0$,

$$\rho_v = 6.85 \times 10^{-5} \left(\frac{\sigma_3}{P_a}\right)^2 - 0.0001995 \frac{\sigma_3}{P_a} + 0.0159,$$

$$\rho_s = 0.000421 \left(\frac{\sigma_3}{P_a}\right)^2 - 0.01256 \frac{\sigma_3}{P_a} + 0.152.$$
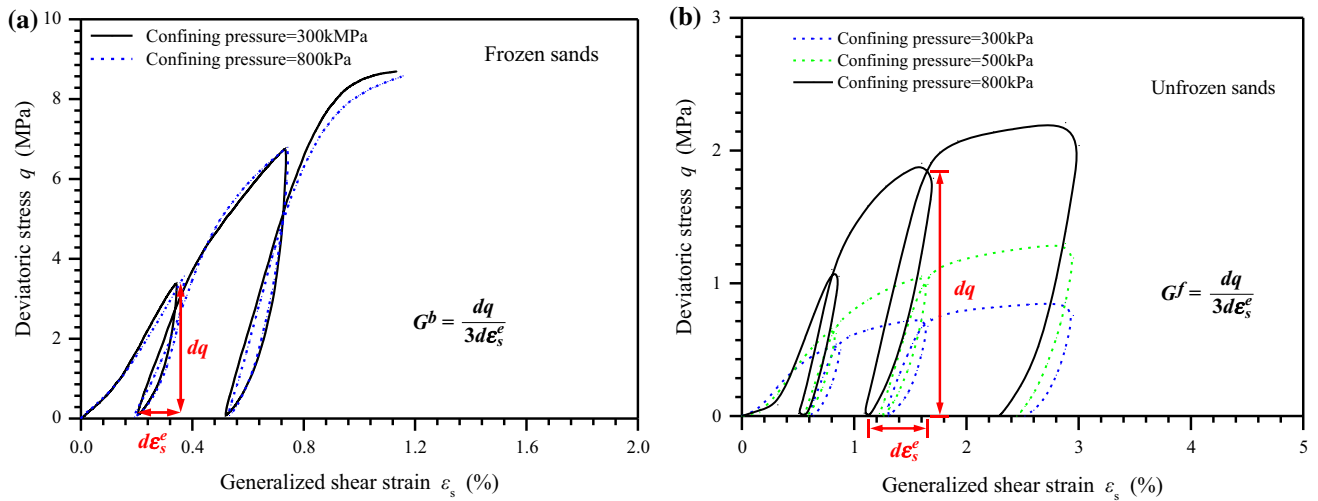

Fig. 13 Loading–unloading–reloading curves of frozen sands and unfrozen sands: **a** frozen sands with confining pressures of 300 and 800 kPa, **b** unfrozen sands with confining pressures of 300, 500, and 800 kPa
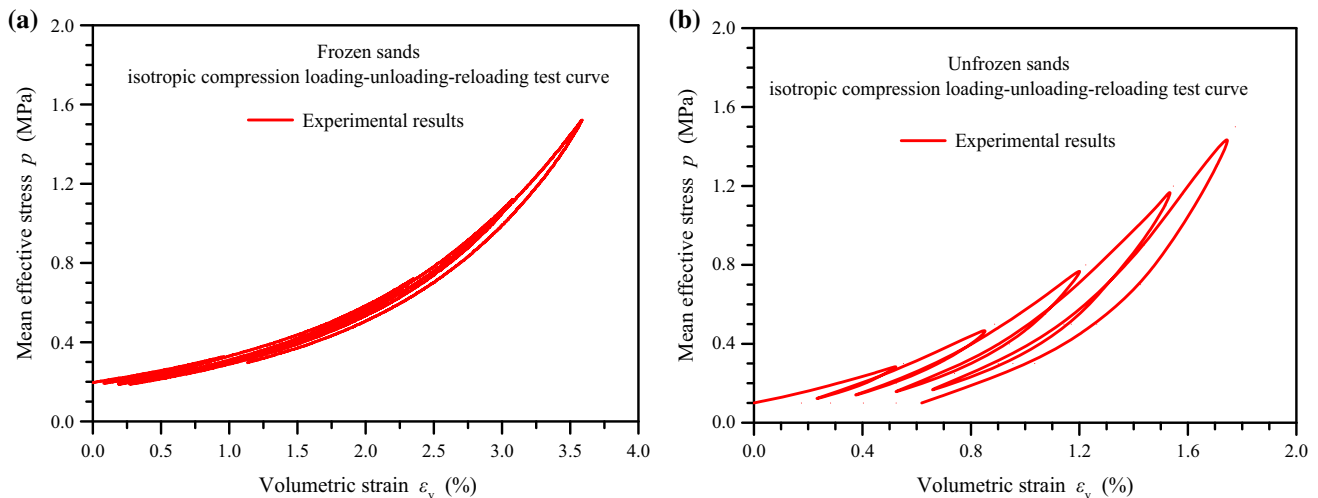

Fig. 14 Isotropic compression loading–unloading–reloading test curve: **a** frozen sands, **b** unfrozen sands
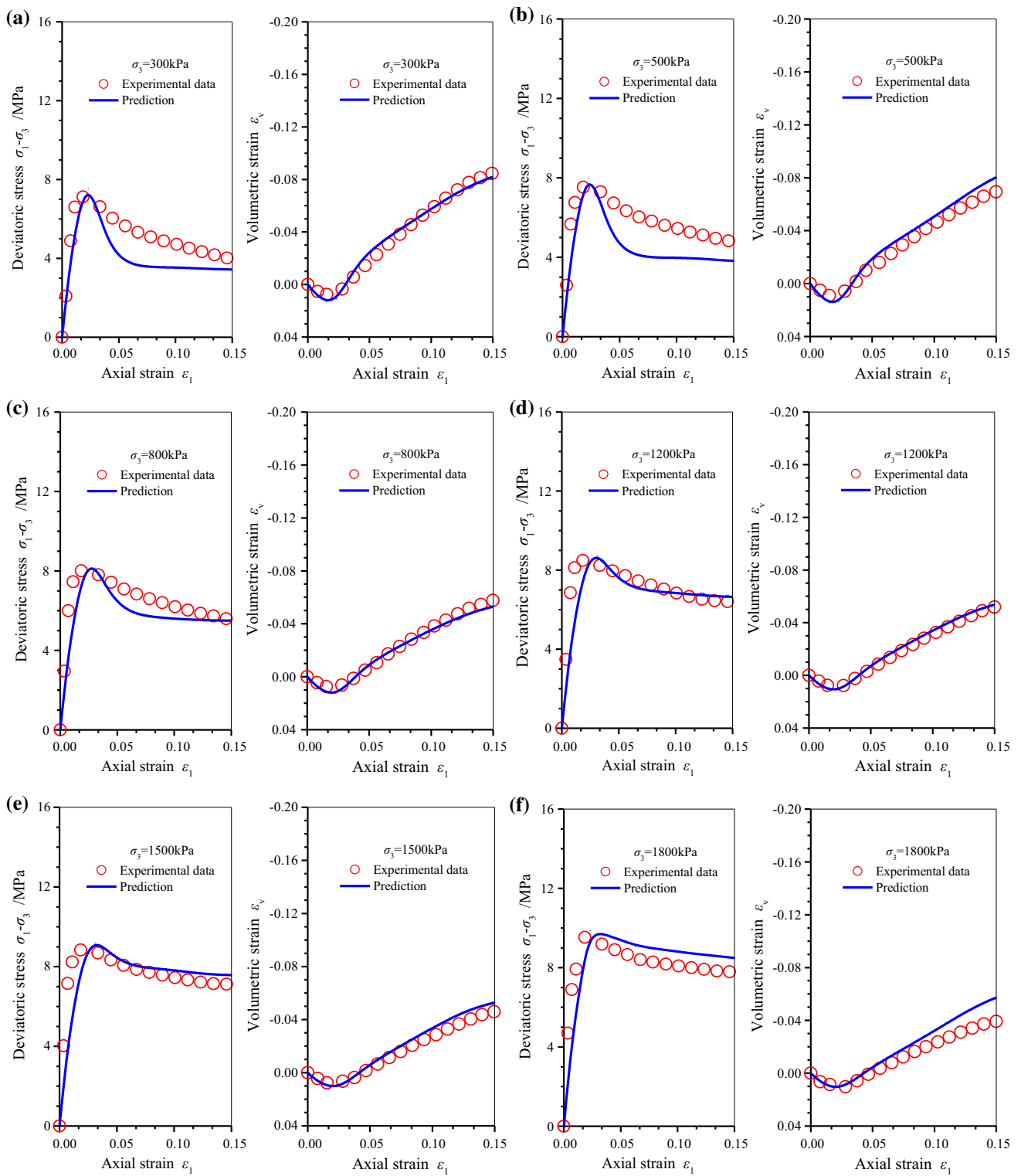
Fig. 15 Comparisons between the laboratory results and predictions of frozen sands

4.4 Model validations

The predicted and measured curves of the deviatoric stress–axial strain and volumetric strain–axial strain of the frozen sands are presented in Fig. 15a–m. Regarding the deviatoric stress–axial strain results, despite some slight discrepancies between the predictions and experimental data at low confining pressures of 300 and 500 kPa, the

proposed binary-medium model can generally represent the strain softening phenomena of the frozen sands. At confining pressures of 800–1800 kPa, the model predictions agree well with the tested results of the deviatoric stress and volumetric strain, particularly for the strain softening and volumetric dilatation behavior.

5 Conclusions

A new constitutive model for frozen sands is proposed based on the homogenization theory framework. The model considers frozen soils as multi-phase composite soils consisting of bonded and frictional elements, and each medium obeys its independent and individual constitutive model. The elastic-based model captures the deformation properties of the bonded elements, and the double hardening elastoplastic model is employed to simulate the behavior of the frictional elements. Moreover, the model considers the interdependency between the binary media by introducing the breakage ratio and local concentration coefficient, that is, the bonded elements are transformed into frictional elements with increasing external loads.

The laboratory tests indicate that the stress–strain behavior of the frozen sands exhibits strain softening and volumetric contraction phenomena followed by dilatancy; their failure characteristics exhibit evident shear bands at a confining pressure below 0 MPa; at higher confining pressures, the centers of the soil samples exhibit bulging. Regarding the unfrozen sands, the stress–stain curves exhibit slight strain softening phenomena at low confining pressures of 300–500 kPa and strain hardening phenomena at 800–1800 kPa. Furthermore, the volumetric strains exhibit contractancy, accompanied by dilatancy at 300–500 kPa; at 1200–1800 kPa, the contraction is continuous. The unfrozen sands are bulged in the center of all tested soil specimens.

The proposed constitutive model conceptualizes the frozen sand specimens as a mixture of bonded and frictional elements; simultaneously, the model considers the nonuniform strain relations between the bonded elements and RVE from a mesoscopic perspective. Breakage ratios are introduced to describe the cementation loss of the ice crystals due to the compressive and shear mechanisms. Finally, an incremental elastoplastic constitutive model is established in the framework of the homogenization technique, and the model parameters are determined based on the laboratory test results of the frozen and unfrozen sands. Compared with the experimental stress–strain results, the proposed model simulates the experimental results of the frozen sands well, including the strain softening, volumetric contraction, and dilatancy.

References

1. Zhou YW, Guo DX, Qiu GQ (2000) Geocryology in China. Science Press, Beijing
2. Lai YM, Xu XT, Dong YH (2013) Present situation and prospect of mechanical research on frozen soils in China. Cold Reg Sci Technol 87:6–18
3. Parameswaran VR (1985) Effect of alternating stress on the creep of frozen soils. Mech Mater 4:109–119
4. Parameswaran VR (1987) Extended failure time in the creep of frozen soils. Mech Mater 6:233–243
5. Tsytovich NA (1985) The mechanics of frozen ground (trans: Zhang CQ, Zhu YL). Science Press, Beijing
6. French HM (1996) The periglacial environment, 2nd edn. Essex, London
7. Zhu ZW, Kang GZ, Ma Y (2016) Temperature damage and constitutive model of frozen soil under dynamic loading. Mech Mater 102:108–116
8. Liu EL, Lai YM, Wong H, Feng JL (2018) An elasto-plastic model for saturated freezing soils based on thermo-poromechanics. Int J Plast 107:246–285
9. Zhao YH, Weng GJ (1996) Plasticity of a two-phase composite with partially debonded inclusions. Int J Plast 12:781–804
10. Zhao YH, Weng GJ (1997) Transversely isotropic moduli of two partially debonded composites. Int J Solids Struct 34:493–507
11. Zhu QZ, Shao JF, Mainguy M (2010) A micromechanics-based elasto-plastic damage model for granular materials at low confining pressure. Int J Plast 26:586–602
12. Zhou MM, Meschke G (2014) Strength homogenization of matrix-inclusion composites using the linear comparison composite approach. Int J Solids Struct 51:259–273
13. Nguyen L, Fatahi B (2016) Behaviour of clay treated with cement & fibre while capturing cementation degradation and fibre failure-C3F Model. Int J Plast 81:168–195
14. Dejaloud H, Jafarian Y (2017) A micromechanical-based constitutive model for fibrous fine-grained composite soils. Int J Plast 89:150–172
15. Zhou MM, Meschke G (2018) A multiscale homogenization model for strength predictions of fully and partially frozen soils. Acta Geotech 13:175–193
16. Lai YM, Jin L, Chang XX (2009) Yield criterion and elastoplastic damage constitutive model for frozen sandy soil. Int J Plast 25:1177–1205
17. Lai YM, Yang YG, Chang XX (2010) Strength criterion and elasto-plastic constitutive model of frozen silt in generalized plastic mechanics. Int J Plast 26:1461–1484
18. Lai YM, Xu XT, Yu WB (2014) An experimental investigation of the mechanical behavior and a hyperplastic constitutive model of frozen loess. Int J Eng Sci 84:29–53
19. Ghoreishian A, Grimstad SA, Kadivar G (2016) Constitutive model for rate-independent behavior of saturated frozen soils. Can Geotech J 53:1646–1657
20. Lai YM, Liao MK, Hu K (2016) A constitutive model of frozen saline sandy soil based on energy dissipation theory. Int J Plast 78:84–113

21. Xu GF, Wu W, Qi JL (2016) Modeling the viscous behavior of frozen soil with hypoplasticity. Int J Numer Anal Meth Geomech 40:2061–2075

22. Zhou ZW, Ma W, Zhang SJ (2016) Multiaxial creep of frozen loess. Mech Mater 95:172–191

23. Loria AF, Frigo B, Chiaia B (2017) A non-linear constitutive model for describing the mechanical behaviour of frozen ground and permafrost. Cold Reg Sci Technol 133:63–69

24. Roscoe KH, Schofield AN, Thurairajah A (1963) Yielding of clays in states wetter than critical. Geotechnique 13:211–240

25. Lade PV, Duncan JM (1975) Elasto-plastic stress-strain theory for cohesionless soil. J Geotech Geoenviron Eng 101:1037–1053

26. Lade PV (1977) Elasto-plastic stress–strain theory for cohesionless soil with curved yield surfaces. Int J Solids Struct 13:1019–1035

27. Zheng YR, Kong L (2005) Generalized plastic mechanics and its application. Eng Sci 7:21–36

28. Yao YP, Sun DA, Matsuoka H (2008) A unified constitutive model for both clay and sand with hardening parameter independent on stress path. Comput Geotech 35:210–222

29. Yao YP, Hou W, Zhou AN (2009) UH model: three dimensional unified hardening model for overconsolidated clays. Geotechnique 59:451–469

30. Yao YP, Zhou AN (2013) Non-isothermal unified hardening model: a thermo-elasto-plastic model for clays. Geotechnique 63:1328–1345

31. Nguyen L, Fatahi B, Khabbaz H (2014) A constitutive model for cemented clays capturing cementation degradation. Int J Plast 56:1–18

32. Hashiguchi K (1980) Constitutive equations of elasto-plastic materials with elastic-plastic transition. J Appl Mech 47:266–272

33. Hashiguchi K, Ozaki S (2008) Constitutive equation for friction with transition from static to kinetic friction and recovery of static friction. Int J Plast 24:2102–2124

34. Nakai T, Hinokio M (2004) A simple elasto-plastic model for normally and over consolidated soils with unified material parameters. Soils Found 44:53–70

35. Liu MD, Carter JP (2002) A structured Cam-clay model. Can Geotech J 39:1313–1332

36. Desai CS (2015) Constitutive modeling of materials and contacts using the disturbed state concept: part 1–Background and analysis. Comput Struct 146:214–233

37. Desai CS (2015) Constitutive modeling of materials and contacts using the disturbed state concept: part 2–Validations at specimen and boundary value problem levels. Comput Struct 146:234–251

38. Liu MD, Carter JP, Desai CS (2003) Modeling compression behavior of structured geomaterials. Int J Geomech 3(2):191–204

39. Yin ZY, Chang CS, Hicher PY, Karstunen M (2009) Micromechanical analysis of kinematic hardening in natural clay. Int J Plast 25:1413–1435

40. Gao Z, Zhao J (2012) Constitutive modeling of artificially cemented sand by considering fabric anisotropy. Comput Geotech 41:57–69

41. Shen WQ, Shao JF (2016) An incremental micro-macro model for porous geomaterials with double porosity and inclusion. Int J Plast 83:37–54

42. Liu EL, Lai YM, Liao MK, Liu XY (2016) Fatigue and damage properties of frozen silty sand samples subjected to cyclic triaxial loading. Can Geotech J 53:1939–1951

43. Ma W, Wu ZW, Zhang LX (1999) Analyses of process on the strength decrease in frozen soils under high confining pressures. Cold Reg Sci Technol 29:1–7

44. Shen ZJ (2002) Breakage mechanics and double-medium model for geological materials. Hydro- Sci Eng 4:1–6 (in Chinese)

45. Shen ZJ, Hu ZQ (2003) Binary medium model for loess. J Hydraul Eng 7:1–6 (in Chinese)

46. Shen ZJ (2006) Progress in binary medium modeling of geological materials. In: Wu W, Yu HS (eds) Trends in geomechanics. Springer, Berlin, pp 77–99

47. Liu EL, Yu HS, Zhou C, Nie Q, Luo KT (2017) A binary-medium constitutive model for artificially structured soils based on the disturbed state concept and homogenization theory. Int J Geomech 17:04016154

48. Liu EL (2005) Binary medium model for structured soils. J Hydraul Eng 36:391–395

49. Liu EL, Zhang JH (2013) Binary medium model for rock sample. Constitutive modeling of geomaterials. Springer, Berlin, Heidelberg, pp 341–347

50. Liu EL, Luo KT, Zhang SY (2013) Binary medium model for structured soils with initial stress-induced anisotropy. Rock Soil Mech 34:3103–3109 (in Chinese)

51. Liu Z, Yu X (2011) Coupled thermo-hydro-mechanical model for porous materials under frost action: theory and implementation. Acta Geotech 6(2):51–65

52. Xu XT, Wang YB, Yin ZH, Zhang HW (2017) Effect of temperature and strain rate on mechanical characteristics and constitutive model of frozen Helin loess. Cold Reg Sci Technol 136:44–51

53. Xu XT, Li QL, Xu GF (2019) Investigation on the behavior of frozen silty clay subjected to monotonic and cyclic triaxial loading. Acta Geotech. https://doi.org/10.1007/s11440-019-00826-6

54. Chang D, Lai YM, Yu F (2019) An elastoplastic constitutive model for frozen saline coarse sandy soil undergoing particle breakage. Acta Geotech. https://doi.org/10.1007/s11440-019-00775-0

55. Xu GF, Wu W, Qi JL (2016) An extended hypoplastic constitutive model for frozen sand. Soils Found 56(4):704–711

56. Cai C, Ma W, Zhou Z et al (2019) Laboratory investigation on strengthening behavior of frozen China standard sand. Acta Geotech 14:179–192

57. Wang JG, Leung CF, Ichikawa Y (2002) A simplified homogenization method for composite soils. Comput Geotech 29:477–500

58. Shen ZJ (1995) A double hardening model for clays. Rock Soil Mech 16:1–8 (in Chinese)

59. Liu EL, Xing HL (2009) A double hardening thermos-mechanical constitutive model for overconsolidated clays. Acta Geotech 4:1–6

60. Liu EL (2010) Breakage and deformation mechanisms of crushable granular materials. Comput Geotech 37:723–730

61. Lemaitre J, Chaboche JL (1970) Mechanics of solid materials. Cambridge University Press, London

62. Lu DC, Du XL, Wang G, Zhou A et al (2016) A three-dimensional elastoplastic constitutive model for concrete. Comput Struct 163:41–55